



SUNRISE III: The Wavefront Correction System

Thomas Berkefeld¹ · Alexander Bell¹ ·
Reiner Volkmer¹ · Frank Heidecke¹ · Tobias Preis¹ ·
Thomas Sonner¹ · Eiji Nakai¹ ·
Andreas Korpi-Lagg²  · Achim Gandorfer²  ·
Sami K. Solanki²  ·
Jose Carlos del Toro Iniesta^{3,4}  ·
Yukio Katsukawa^{5,6,7}  · Pietro Bernasconi⁸  ·
Alex Feller²  · Tino L. Riethmüller²  ·
Alberto Álvarez-Herrero^{9,4}  · Masahito Kubo⁵  ·
Valentín Martínez Pillet¹⁰  · H. N. Smitha²  ·
David Orozco Suárez^{3,4}  · Bianca Grauf² ·
Michael Carpenter⁸

Received Tuesday 10th February, 2026; 01:33

© The author(s) ••••

✉ A. Korpi-Lagg
lagg@mps.mpg.de
T. Berkefeld
thomas.berkefeld@leibniz-kis.de
A. Gandorfer
gandorfer@mps.mpg.de
S. K. Solanki
solanki@mps.mpg.de
J. C. del Toro Iniesta
jti@iaa.es
Y. Katsukawa
yukio.katsukawa@nao.ac.jp
P. Bernasconi
pietro.bernasconi@jhuapl.edu
A. Feller
feller@mps.mpg.de
T. L. Riethmüller
riethmuller@mps.mpg.de

- ¹ Institut für Sonnenphysik (KIS), Georges-Köhler-Allee 401a, 79110 Freiburg, Germany
- ² Max-Planck-Institut für Sonnensystemforschung, Justus-von-Liebig-Weg 3, 37077 Göttingen, Germany
- ³ Instituto de Astrofísica de Andalucía, CSIC, Glorieta de la Astronomía s/n, 18008 Granada, Spain

Abstract This paper describes the wave-front correction and image stabilisation system (CWS) developed for the SUNRISE III balloon-borne telescope, and provides information about its performance as measured during the integration into the telescope and during the 2024 science flight. The fast image stabilisation is done by a correlation tracker (CT) and a fast tip-tilt mirror, low order aberrations such as defocus and coma are measured by a six-element Shack-Hartmann wavefront sensor (WFS) and corrected by an active telescope secondary mirror for automated focus and manual coma correction. The CWS is specified to deliver a stabilised image with a precision of 0.005 arcsec (rms). The autofocus adjustment is specified to maintain a focus stability of 0.01 waves in the focal plane of the CWS.

Keywords: Balloon-borne Telescope; Instrumentation; Adaptive Optics; Wavefront Sensing; Shack Hartmann; Tip-tilt Correction; Image Stabilisation; SUNRISE, Correlation Tracking

1. Introduction

After two successful science flights in 2009 and 2013 (see Solanki et al. 2010, 2017), and a failed attempt in 2022, the SUNRISE balloon-borne solar observatory (see Barthol et al. 2011; Gandorfer et al. 2011; Berkefeld et al. 2011; Martínez Pillet et al. 2011) successfully completed its third science flight in July 2024 (Korpi-Lagg et al. 2025), again from Kiruna, Sweden to northern Canada. Stratospheric balloon-borne telescopes have two fundamental advantages over ground-based telescopes: they permit UV observations and they provide a seeing-free image quality over the full field of view (FoV) for in principle long periods of time. However, pointing to the Sun and tracking a feature on the solar surface is a challenging task, especially for a telescope hanging under a balloon that is driven by stratospheric winds at an altitude of 36 km. In addition to the apparent (diurnal and seasonal) motion of the Sun, there are a number of oscillatory modes that may be induced by variable winds in the stratosphere, and taken up by the balloon-gondola system. The resulting gondola pendulum motion of a few degrees must be reduced to a few milliarcseconds to provide diffraction-limited observations.

The gondola pointing system for SUNRISE III has been built by the Johns Hopkins University Applied Physics Lab (see Bernasconi et al. (2025)) and provides the coarse

⁴ Spanish Space Solar Physics Consortium (S³PC)

⁵ National Astronomical Observatory of Japan, 2-21-1 Osawa, Mitaka, Tokyo 181-8588, Japan

⁶ Department of Astronomy, The University of Tokyo, 7-3-1, Hongo, Bunkyo-ku, Tokyo 113-0033, Japan

⁷ The Graduate University for Advanced Studies, Sokendai, Shonan Village, Hayama, Kanagawa 240-0193, Japan

⁸ Johns Hopkins University Applied Physics Laboratory, 11100 Johns Hopkins Road, Laurel, Maryland, USA

⁹ Instituto Nacional de Técnica Aeroespacial (INTA), Ctra. de Ajalvir, km. 4, E-28850 Torrejón de Ardoz, Spain

¹⁰ Instituto de Astrofísica de Canarias, Vía Láctea, s/n, E-38205 La Laguna, Spain



Figure 1. SUNRISE III before launch in 2024

image stabilisation to within a few arcseconds. The second (fine) level of image stabilisation to within five to ten milliarcseconds is performed inside the post focus unit by the combination of a correlating wavefront sensor (CWS) and a fast tip-tilt mirror which measure and correct the residual image jitter, respectively. Furthermore, the CWS is also able to sense coma and focus. This information is used for in-flight telescope alignment using the secondary mirror M2.

The CWS was completely redesigned for the SUNRISE III flight in 2022 for the following reasons:

- due to a completely new suite of science instruments for SUNRISE III, the CWS operates at 640 nm instead of 500 nm as for SUNRISE I and II, which would have led to a decreased measurement accuracy as a result of the longer wavelength and the lower contrast of the solar granulation. Adding a fast correlation tracker to the CWS compensates the loss of accuracy, but required a more powerful realtime control computer.
- advances in computing technology, i.e. changing the realtime control computer, allow for a simplified electronics setup and lower latencies in the realtime control loop of the tip-tilt correction, leading to an improved system performance even with the slower (but necessary) SUNRISE III tip-tilt mount, i.e. for tip-tilt, the 0-db correction bandwidth increases from 90 Hz to 130 Hz.
- in 2022 the CWS flight hardware of SUNRISE I and II would have been more than 15 years old. Problems with batteries buffering some BIOS settings in the CWS realtime-computer added to the decision for using a new control computer.

Compared to the 2022 flight attempt, only minor software updates were applied for the 2024 science flight.

Section 2 lists the basic requirements and systems specifications, section 3 explains the optical design, section 4 deals with the wave-front correction algorithms and software. The electronics and tip-tilt hardware are described in section 5, followed by a performance analysis and a short conclusion.

2. System Requirements / Specifications

Table 1 lists the requirements for the basic parameters of the Correlating Wavefront Sensor (CWS). The main differences to SUNRISE I and II are the operating wavelength and input voltage, which required changes in the optics and electronics. Although these

Table 1. CWS System Requirements

Parameter	Requirement
measured aberrations	tip-tilt, focus, coma
operating wavelength	640 nm
uninterrupted locking duration	> 4 hours
residual TT correction accuracy	< 5 milliarcseconds RMS
TT correction bandwidth (0db)	> 100 Hz
autofocus accuracy	< $\lambda/100$ RMS on granulation
coma measurement accuracy	< $\lambda/100$ RMS on granulation
TT correction range on sky	60 arcseconds
input voltage	24V
allowed power consumption at input	80 W
allowed mass (excl. TT mirror)	max. 10 kg
temperature range op / non-op [$^{\circ}$ C]	0... 30 / -40... 40
pressure range	3... 1000 mbar

requirements are very similar to the ones of SUNRISE I and II, numerous modifications and innovations were necessary to interface with the new gondola, and to benefit from the damping of the pendulum motion with the gondola roll wheel. In addition, the science focus for SUNRISE III changed to obtaining several hour-long time series, requiring optimizations to achieve an uninterrupted locking duration of > 4 hours.

3. Optical Design

3.1. Telescope

The core component of the SUNRISE observatory is a 1 m Gregory-type telescope (Barthol et al. 2011). The parabolic primary mirror M1 ($f/2.42$) provides a full disk image in its focal plane. Here a field stop, which is also a heat rejection device, reflects and absorbs 99% of the sunlight. Only a field of view of 200 arcsec passes to the elliptical

secondary mirror M2 which delivers a $f/24.2$ focus via two folding mirrors to F2, where a field stop is placed. Here, also several calibration targets, as well as a shutter for dark exposures can be inserted into the beam. An Offner relay creates a real image of 25 mm diameter of the system pupil on a fast tip-tilt mirror for compensating image jitter (see Korpi-Lagg et al. 2025, for a detailed description). Taking into account the maximum stroke of the tip-tilt mirror of 60 arcsec per axis, the maximum unvignetted science field of view has an edge length of 80 arcsec. The light distribution of SUNRISE III feeds three scientific instruments:

- SUSI (SUNRISE Spectropolarimeter and Imager), a full Stokes spectropolarimeter working from 309 to 417 nm, with slitjaw imaging and phase diversity capability for spectrum/slit and image reconstruction to remove remaining static aberrations (Feller et al. 2025),
- TuMAG (Tunable Magnetograph), an imaging full Stokes spectropolarimeter working at 517 and 525 nm and phase diversity capability (del Toro Iniesta et al. 2025), and
- SCIP (SUNRISE Chromospheric Infrared spectro-Polarimeter), a full Stokes spectropolarimeter working at 854 and 770 nm with slitjaw imaging (Katsukawa et al. 2025).

The fourth channel feeds the CWS which is responsible for the high speed tip-tilt correction, slow autofocus and coma measurement (coma is corrected manually).

3.2. CWS

In contrast to SUNRISE I and II, where the CWS had a six-element Shack-Hartmann wavefront sensor (WFS) for fast tip-tilt correction, slow autofocus and coma measurement, SUNRISE III was upgraded with a correlation tracker (CT) for the fast tip-tilt-correction. The WFS is now only used for the slow autofocus and coma measurement. For the fast tip-tilt-correction this has the advantage of an improved tip-tilt measurement accuracy by using diffraction limited sampling of the full aperture resolution and a much faster readout (7 kHz instead of 1.7 kHz) of the CT camera which results in an increased correction bandwidth (130 Hz instead of 90 Hz).

Figures 2 and 3 show the optics of the CWS, table 2 lists its parameters. The entrance focus unit of the CWS (the light enters from the left) includes a dark stop, a pinhole and a field stop which limits the field of view of the incoming $f/24$ beam to 13 arcsec on sky. The following collimator lens ($f=100$ mm) collimates the beam. A bandpass filter with a central wavelength of 640 nm and a bandpass of 10 nm limits the photon flux and the wavelength range to minimise chromatic aberrations. Next, a beam splitter plate transmits 10 % of the light to the WFS and reflects 90 % to the CT. The splitting ratio reflects the much faster frame rate / lower exposure time of the CT as compared to the WFS.

Hang tests in Göttingen in 2021 showed that the light throughput of the telescope and the transfer path was higher than estimated. A neutral density filter was added in the common CWS path to lower the light level by a factor of four (not shown in Figures 2 and 3).

For both channels, a pupil of diameter 4.1 mm is created by the collimator lens with a focal length of $L = 100$ mm. In the WFS channel, a 6-element lenslet ($L = 78$ mm) at the pupil position creates six subimages. The subsequent $\times 0.6$ magnifying stage ($L = 125$ mm + $L = 75$ mm) leads to the final 0.2 arcsec/pix on the WFS camera. The six subapertures allow to measure coma, defocus and tip-tilt (the latter was only used for sun-pointing tests from ground). In the CT channel, the reimager lens ($L = 125$ mm) leads to a 1.25 magnification. Both channels have diffraction-limited sampling (assuming the $1.22\lambda/D$ definition) with respect to their respective effective aperture size.

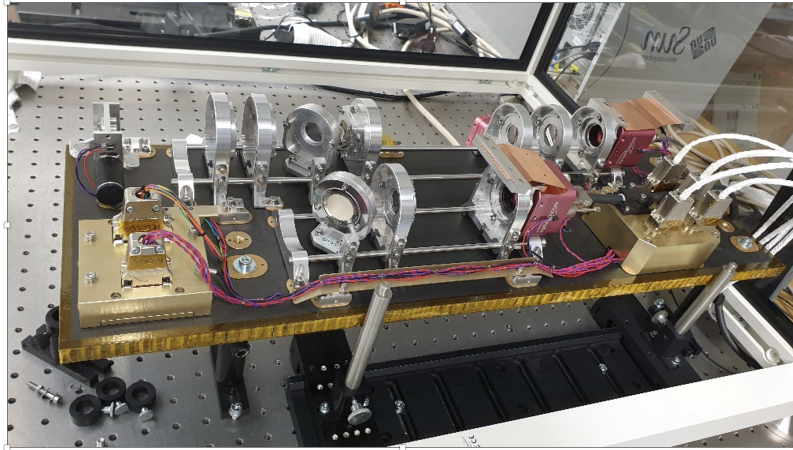


Figure 2. Optics (O-Unit) of the CWS. The light is coming from the left.

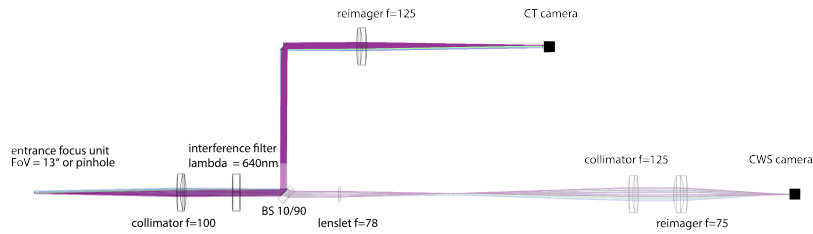


Figure 3. Optics design of the CWS. The light is coming from the left.

3.3. Tip-Tilt Mirror

The tip-tilt mirror used for the fast image stabilisation is situated at a pupil image of 25 mm in diameter. Its mirror blank has a diameter of 30 mm. The mirror is driven by a two-axis piezo ceramic actuator from Physik Instrumente (S-330.8). This piezo drive fulfills all requirements for the SUNRISE image stabilisation (range on sky > 60 arcseconds and high dynamics, i.e., a resonance frequency of 700 Hz (channel 1) and 1200 Hz (channel 2) using the SUNRISE III tip-tilt mirror cell). The piezo actuators have

Table 2. Parameters of the WFS and CT inside the optics unit of the CWS.

	WFS	CT
# of subapertures (total)	6	1
measured aberrations	tip-tilt, focus, coma	tip-tilt
subaperture size projected on M1 [m]	0.33	1
FoV on sky [arcsec]	13	6.7
pixel scale [arcsec/pix]	0.2	0.07
# of pixels used for crosscorrelation	64×64	96×96
camera (manufacturer = Photonfocus)	MV1-D1024E-80-G2	MV1-D1024E-160-CL
typical framerate [Hz]	500	7000

a total tilt range of approx. 6 mrad (corresponding to ± 30 arcsec on sky) using a voltage range of 7...93 V. The minimal step size corresponds to $0.1 \mu\text{rad}$ (0.001 arcsec on sky).

Both, the design of the SUNRISE III tip-tilt mirror cell, and the mechanical holder of the piezo actuator inside the post-focus instrumentation platform had to be changed with respect to the SUNRISE I and II designs. The new SUNRISE III tip-tilt mirror cell was designed by MPS with the main goal of maintaining the flatness of the mirror surface up to a temperature of 100°C under solar load. MPS built an additional mechanical adapter made of titanium with INVAR flex blades, a concept similar to the mirror interface used inside the image stabilisation of the High Resolution Telescope (HRT, see Gandorfer et al. (2018)) of the Polarimetric and Helioseismic Imager (PHI) (Gandorfer et al. 2018; Solanki et al. 2020) on board Solar Orbiter (Müller et al. 2020). This design preserves the optical surface quality of the tip-tilt mirror at the expense of a higher oscillating mass - thus reducing the eigenfrequency of the tip-tilt-system which leads to a lower tip-tilt correction bandwidth and ultimately lower tip-tilt correction quality. MPS also replaced the mechanical interface of the piezo actuators to the structure to fit into the spatial constraints given by the new optics layout.

Figure 4 shows a picture of the tip-tilt mirror cell, the piezo actuator and its mechanical interface to the structure.

4. Wave-Front Correction

4.1. Overview

The main components of the wave-front correction system are the following devices: the Shack-Hartmann wave-front sensor, the correlation tracker, each with a fast camera, the fast tip-tilt mirror (7000 Hz update rate), the slow secondary mirror M2 (0.1 Hz - 0.01 Hz update rate) and the the control computer which connects the two sensors to the tip-tilt mirror and M2 (via the CWS communication software CW-COM (see Sec. 4.4) and the ICU).

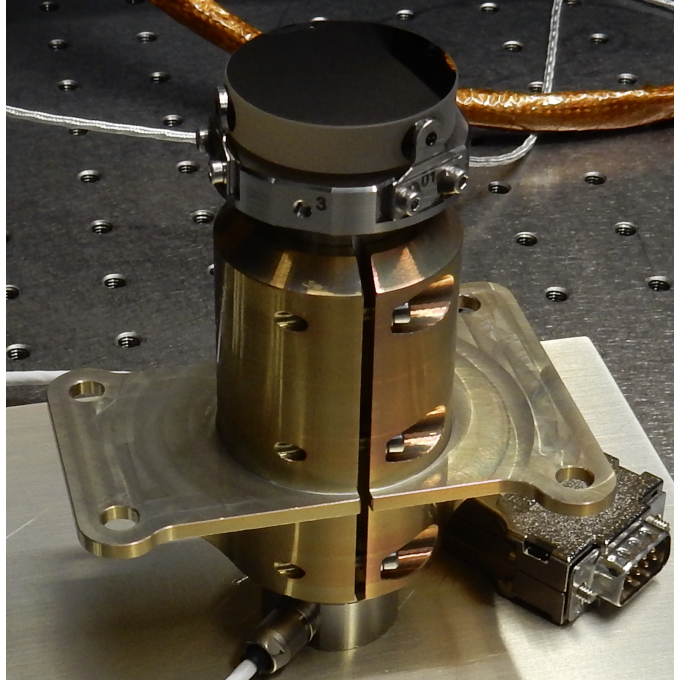


Figure 4. Picture of the tip-tilt mirror cell, the actuator, and its mount.

The telescope secondary mirror, M2, has high alignment tolerances with respect to M1, since a shift of M2 in axial (z) direction by, e.g., $16\ \mu\text{m}$ leads to a focus wavefront error of 100 nm RMS in the science focus. Therefore, M2 is mounted on a motorized xyz stage that is controlled by the CWS to ensure proper alignment. Lateral (xy) misalignment causes coma and image shift, while axial (z) misalignment causes spherical aberration but was found not be critical, and defocus.

4.2. Wave-Front Reconstruction

Both the CT sensor and the Shack-Hartmann sensor use cross-correlation with a reference image for determining the image shift of the respective sub-aperture (the CT has only one sub-aperture which is the full aperture). Since the solar structures evolve, the cross correlation reference image has to be updated regularly, i.e. as fast as the solar structure evolves at a given spatial resolution. The reference images in both sensors were updated every 10 seconds.

The data reduction of the sub-aperture pixel data is done in a very similar way as in the solar AO system KAOS at the GREGOR solar telescope on Tenerife (Berkefeld et al. 2012).

The wavefront reconstruction is also similar to the AO-system at the GREGOR solar telescope. The aberrations that need to be sensed determine the number of Shack-Hartmann sub-apertures:

-
- Tip-tilt: needs to be corrected in closed loop, is sensed by the correlation tracker.
 - Defocus (caused by M2 or M3/M4 axial misalignment): needs to be corrected in a slow closed/automatic control loop to cope with focus drifts due to, e.g., temperature changes.
 - Coma (caused by M2 lateral misalignment): In principle, coma can be removed in closed loop by a lateral movement of M2. However, since a lateral movement of M2 produces 400 waves of tip-tilt for each wave of coma¹, a closed-loop coma-correction would have a negative impact on the tip-tilt performance. Instead, the coma is corrected manually prior to starting observation sequences. The initial alignment of the telescope ensures that only slight lateral M2 adjustments have to be made, so that no vignetting of the F2 field stop by the F1 field stop occurs.
 - Spherical aberration (SA, caused by M2 axial misalignment): Although it is in principle possible to remove both, defocus and SA, simultaneously with M2 and M3/M4, an analysis of the optical errors showed that the amount of spherical aberration induced by a defocus of M2 is well within the range measurable by the phase diversity setups of the science instruments. Therefore it was sufficient to statically align M2 and M3/M4 prior to the flight and correct the in-flight defocus with M2 only, and no sensing of SA was required.
 - Other higher order errors (such as triangular coma due to the M1 support): Interferometric measurements have shown that they have only minor contributions to the overall wavefront error. Furthermore, SUSI (UV) and TuMAG (VIS) can apply phase diversity techniques to remove remaining small aberrations during post-facto processing. SCIP at its NIR wavelength range does not require this.

The reconstruction matrix for the tip-tilt mirror is the SVD-inverted measured interaction matrix between xy-shifts and the actuators. The tip-tilt servo is a PID type (proportional + integral + differential), running at 6-7 kHz loop frequency of the CT sensor.

Modal aliasing analysis shows that a six sub-aperture WFS is sufficient to sense defocus and coma (three modes). The condition number of the corresponding modes-to-shifts matrix which links the modal coefficients to the Shack-Hartmann WFS shifts is < 5 , i.e. well below 10 which is often used as a limit for numerical stability in AO wavefront reconstruction.

The corresponding reconstruction matrix has been pre-calculated via Zernike polynomials and scaled according to the WFS pixel scale. An additional conversion factor according to the M2 step size is applied inside the Instrument Control Unit. Since the focus drift due to varying zenith angles occurs on timescales of minutes, M2 receives a time-averaged signal. The averaging time is two seconds (1000 frames), guaranteeing a reduction of the measurement error below 0.05 rad RMS for defocus and coma, but also allowing a fast activation of the autofocus when starting observations. Focus signals below a certain threshold (typically around $5 \mu\text{m}$) were not applied to limit the number of M2-z movements, since they would cause an additional short pulse of lateral image motion.

¹

One wave (640 nm) rms of tip tilt aberration corresponds to 0.53 arcsec of image shift.

4.3. Measurement Accuracy

Optics theory, experience in solar AO systems and also the equation given by Michau et al. (1991) show that the measurement accuracy of a correlating Shack-Hartmann sensor depends on the following properties:

- Image contrast and its spatial power spectrum, i.e. the signal,
- sub-aperture diameter,
- observing / sensing wavelength,
- pixel scale / sampling,
- number of pixels per cross correlation field, and
- noise (shot noise, camera readout noise and digitisation noise).

The SUNRISE CT-sensor works at 640 nm and uses the full 1 m telescope aperture, producing a spatial resolution of 0.16 arcsec, using the $1.22 \lambda/D$ definition. The slight oversampling (0.07 arcsec/pixel) and cross correlation field of 96×96 pixels yield a field of view of 6.7 arcsec. To calculate the RMS intensity contrast as seen by the wave-front sensor, the original power spectrum of the solar granulation has to be multiplied by the modulation transfer function of the (sub-)aperture. This reduces the original granulation contrast of 11 % at 640 nm, as measured by the Swedish Solar Telescope using Adaptive Optics and image reconstruction (at 630 nm, see Scharmer et al. 2010) to 8 % for the CT (theoretical contrast), and to 5 % for the WFS (theoretical contrast). Image 5 is a live screenshot of granulation taken during the SUNRISE III flight, showing both the CT and the WFS image plus their respective correlation function. The image contrast was 6.6% (CT) and 4.9% (WFS).



Figure 5. Screenshot of granulation showing the CT and WFS image plus their respective correlation function taken during the SUNRISE III flight.

Michau et al. estimated that the measurement noise variance $\sigma_{\text{snr},\lambda}^2$ (in λ^2) for a critically sampled, correlating single aperture is

$$\sigma_{\text{snr},\lambda}^2 = \frac{5 m^2 \sigma_{\text{noise}}^2}{4 n^2 \sigma_{\text{signal}}^2}, \quad (1)$$

where m denotes the width of the autocorrelation function in pixels, σ_{noise} the noise in electrons standard deviation, n the number of pixels across the cross correlation field of view (96 for the CT) and σ_{signal} the image contrast in electrons standard deviation.

The noise has three main contributors: for the photon noise we assume a number of 160000 e^- (photo electrons) per pixel (80 % full well capacity), yielding 400 e^- of shot noise. The 8-bit digitization leads to a noise of $200000 e^- / 256 = 800 e^-$ peak-to-peak (LSB) which corresponds to about 462 e^- RMS ($800/\sqrt{3}$). The third contributor is the readout noise of 220 e^- as specified by the camera manufacturer, resulting in a total noise of 650 e^- standard deviation (assuming that the three noise sources are independent of each other).

For the signal we use 80 % of the full well capacity again and a contrast of 6.6% (CT, corresponding to an average signal of ca 10500 e^- / pixel) and 4.9% (WFS, corresponding to a signal of 7800 e^-), respectively. Using Eq. (1) and subsequent conversion from a wave-front error (in λ) to a pointing error (tip-tilt error, in arcsec), the RMS measurement error becomes

$$\sigma_{\text{snr},\lambda} = 0.0007 \cdot m [\lambda], \text{ corresponding to } \sigma_{\text{snr,tip\&tilt}} \approx 0.00038 \cdot m [\text{arcsec}] \quad (2)$$

for the CT's 1 m aperture and

$$\sigma_{\text{snr},\lambda} = 0.0015 \cdot m [\lambda] \quad (3)$$

for a WFS single 33 cm subaperture.

For ground-based adaptive optics wavefront sensing on granulation, the correlation function is usually 4 pixels wide (for a typical subaperture size of 8-10 cm and seeing in the same ballpark). However, the width of the SUNRISE III WFS correlation functions m for granulation is ca 5-6 pixels wide, the width of the CT correlation function is ≈ 12 pixels wide. The increased widths of the correlation functions for the SUNRISE III larger WFS and CT apertures resemble the decreasing solar signal at increasing spatial frequencies. When locking on sunspots the width of the correlation function can get even larger, however, the overall measurement error decreases due to the increased image contrast as compared to granulation.

The final CT measurement error for a single measurement when locking on granulation ($m = 12$) becomes

$$\sigma_{\text{snr,tip\&tilt}} \approx 0.0045 [\text{arcsec}]. \quad (4)$$

Due to the temporal averaging / oversampling of the CT control loop with respect to the correction bandwidth (7 kHz as compared to 130 Hz) the effective measurement error is significantly lower, but hard to quantify.

For the WFS (single subaperture), using $m = 6$ results in

$$\sigma_{\text{snr},\lambda} = 0.009 [\lambda]. \quad (5)$$

In theory, even without spatial (6 subapertures available, only 2 subapertures required for focus detection) or temporal averaging the accuracy of the focus measurement is already better than the focusing precision given by the M2 mechanical resolution (1 μm). Nevertheless, temporal averaging over 1000 frames (2 sec) plus a minimum threshold to avoid lateral image jitter by the focus mechanism was used for SUNRISE III.

4.4. Real Time Control / Software

This section deals with the CWS flight control software running on an embedded Intel-based micro-computer. The conduction-cooled computer features a quad-core Intel i7 processor, 32 GB RAM and connects to one camera using Ethernet while the second camera is connected via a frame-grabber card running the camera link protocol. The CWS-software is divided into two parts: the first (CW-AO) handles the fast tip-tilt correction loop plus the slow autofocus correction/coma measurement. The second (CW-COM) handles the communication to the ICU (commanding and telemetry). This division allowed using a variant of the Adaptive Optics control software used at the GREGOR Solar Telescope on Tenerife (Berkefeld et al. 2012) as CW-AO. Equally important, the CW-COM software could be developed independently.

4.4.1. CW-AO

In order to achieve a high tip-tilt system bandwidth for the fast tip-tilt correction, the delays in the control loop have to be as small as possible. Listed below are the delays of the correction:

- 30 - 50 μs = half of the exposure time. The exposure time depends on the target (sunspot, quiet sun) and on the target position (disk center, close to the limb).
- 75 μs = readout time, according to the camera manufacturer
- 75 μs = compute time, mostly for the shift determination of the 96×96 pixel correlation field. In order to achieve a low compute time, the data reduction is vectorised (auto-vectorisation by the compiler), the cross-correlation uses the FFT library *FFTW*, measured with the computer's high resolution timer
- 50 μs = output + digital to analog (DA) conversion, given by the output data rate and the DA electronics specification
- 1100 μs = tip-tilt mirror settling time to 90% including high voltage amplifier (measured time between input signal at the high voltage amplifier on one channel and the induced voltage at the piezo of the other channel)

An additional 70 μs for the average hold time (limited sampling frequency, 1/7 kHz/2) has to be added to the total delay of ca. 1.4 ms between the occurrence of a disturbance and its correction. One CPU core is assigned exclusively to the fast tip-tilt control loop in order to minimise temporal jitter, which was measured to be 1-2 μs .

4.4.2. CW-COM

Running on the same computer as CW-AO, the CW-COM software handles the communication to the ICU and (on ground) the CWS Electronic Ground Support Equipment (EGSE), freeing the realtime control software from these tasks.

CW-COM controls CW-AO by a state machine which handles special tasks required by the time-line driven operation of the instruments. Amongst these the autolock mode is the most important, which guarantees that lock for the focus as well as for the image

stabilisation are achieved automatically during flight and are reestablished in case one or both of them are lost. This is important for the above mentioned time-line driven operation and for the case that stable telemetry to the SUNRISE gondola is lost during flight.

5. Electronics

5.1. Overview

The CWS electronics for SUNRISE III differ significantly from the electronics for SUNRISE I and II - the proximity electronics box (PEB) has disappeared and its contents have been split between the E-Unit and the O-Unit. As only the CWS entrance focus unit remains from the original three mechanisms, its motor controller could be integrated into the O-Unit and is directly connected to the E-Unit via RS422. The E-Unit now also contains the amplifier with 100 V charge pump for the tip-tilt piezo drive and the power supply for the entire CWS electronics and the VPX6 computer board, which now also handles all communication tasks that were outsourced to a smaller computer board for SUNRISE I and II. Furthermore, the system voltage changed from 24 V DC to 12 V DC, which allowed an isolated 24 V to 24 V DC/DC converter to be eliminated. To summarise, the electronics architecture has become simpler and more powerful (see schematics in Fig. 6).

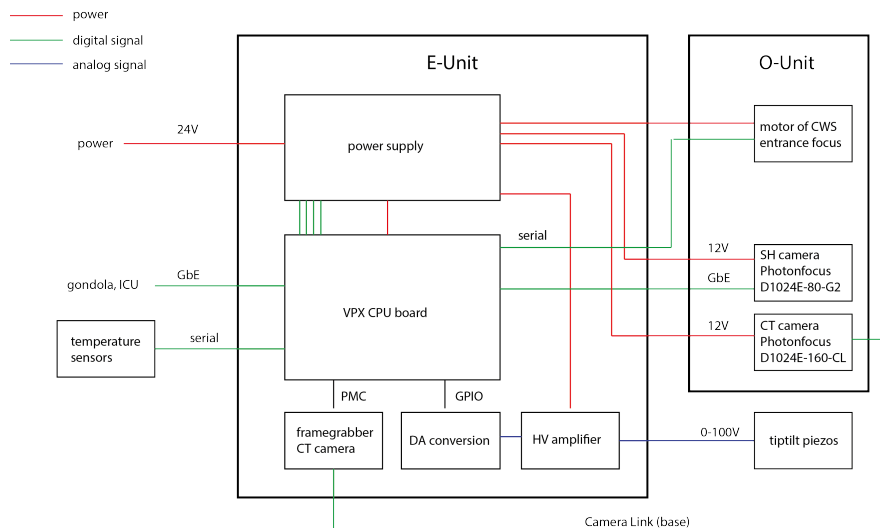


Figure 6. Electronics and harness layout.

5.2. Main Electronics Unit (E-Unit)

The main components of the E-unit are shown in Figure 7: The TT (tip-tilt) amplifier board has the identical circuit technology as in SUNRISE I and II. Only the form factor

has been adapted for the placement in the E-Unit. In addition, the amplifier has a digital-to-analog converter (DAC) board with two 16-bit AD5541 converters at the input. The power for all components of the CWS is provided from the DC/DC converter board that has several voltage levels with different requirements on current and/or ripple. Power management is much simpler as compared to SUNRISE I and II. The VPX6 computer board only has to take care of switching the TT amplifier with its 100 V charge pump on and off. All other components are supplied immediately as soon as the ICU supplies power to the CWS. The VPX6-1959 Single Board Computer with its Quad-Core i7-5850EQ processors at 2.7 GHz, made by Curtiss Wright, handles all computational tasks: CWS correction control loop, all communication tasks via Ethernet, PCI Mezzanine Card (frame grabber PMC DV C-Link), serial interfaces and IOs, i.e., no additional computer is required. A parallel 7-bit real-time output drives the two 16-bit 5541 DA converters to the TT high voltage amplifiers, which reduced the output time from 119 μ s to 50 μ s as compared to SUNRISE I and II.

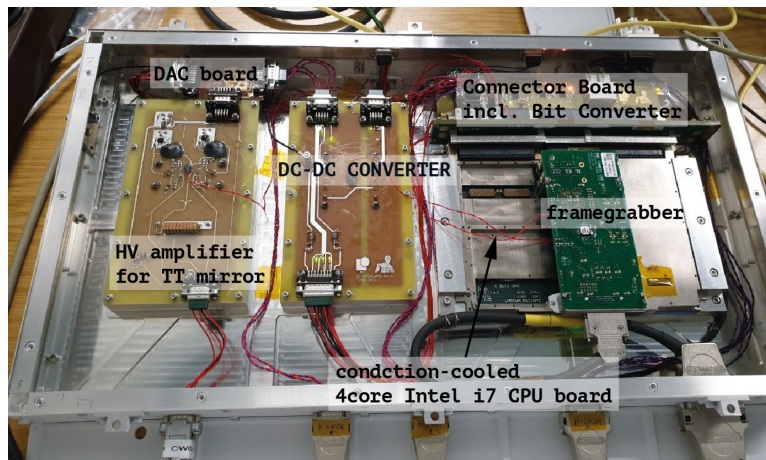


Figure 7. Opened E-unit with unmounted connectors: amplifier with DAC board (on the left), power supply (in the middle), VPX6 computer board with frame grabber (the green one) and the connector board at the back side.

5.3. Electronics in O-Unit

The O-Unit contains two cameras, one motor controller and its DC-servo motor as main electronic components. The MV1-D1024E-3D02-160-G2 Ethernet camera is connected directly to the VPX6 computer board via Ethernet. It is supplied with 12 V DC and its power requirement is less than 4.8 W. The MV1-D1024E-160-CL Camera Link camera is connected to the frame grabber. It is also supplied with 12 V and its power consumption is less than 3.2 W. The motor controller in the box is a MCBL3002 PRS motion controller made by Faulhaber. The Faulhaber controller, which is also supplied with 12 V, has an RS232 interface - an RS232-to-RS422 converter IC is included on the motor controller board in the box to ensure differential data transmission to the RS422 interface of the VPX6 computer board. The controlled 2036U024B K1155 brushless DC servo switches the state of the CWS entrance focus unit between dark stop, pinhole and field stop.

5.4. Tip-Tilt Mirror

For the tip-tilt correction a two-axis piezo ceramic actuator from Physik Instrumente is used (S-330.8). This piezo drive fulfills the requirements for the SUNRISE image stabilisation (high acceleration, fast response to set points and small increments). The piezo actuators have a total tilt range of approx. 10 mrad @ -20. . . 120 V, of which the range 7. . . 93 V is used, corresponding to ca 6 mrad. The minimal step size given by the 16 bit digitization is 0.1 μ rad.

For all SUNRISE balloon flights, an in-house development for the piezo amplifier was necessary because no suitable off-the-shelf component was available. The PICO IRF charge pump, which supplies the 100 V for the amplifier, is supplied with 12 V for SUNRISE III (a PICO IRA charge pump for 24 V DC was used for SUNRISE I and II). The AB class amplifier has two channels, each with a complementary pair of mosfet transistors. The form factor had to be adapted for installation in the e-unit.

Table 3. Amplifier Characteristics.

Channel 1	7 V...93 V
Channel 2	7 V...93 V
Channel 3	100 V fixed
IRF charge pump supply	8 V...24 V \rightarrow 100 V (max. 10 W)
Push-pull power stage	max. 2 * 5 W @ 60 Hz full scale driven
Pre-amplifier	0 V..5 V \rightarrow 0 V..100 V
DA converter interface	SPI to 5x7-bit parallel (via micros)
DA converter update max. frequency	20 kHz
DA converter resolution	16 bit
Voltage scale	97.6 V / 65535 = 1.489 mV / LSB
Dynamic amplifier range	86 V
Tip-tilt range (on sky)	60 arcsec
Tip-tilt resolution (on sky)	0.001 arcsec

5.5. Thermal and Environmental Design

At flight altitude the atmospheric pressure is about 5 mbar. To dissipate the power effectively by thermal radiation, the cooling elements have an allocated radiation area, and the cooling design has to ensure that the heat is transmitted to that area. A detailed thermal analysis of SUNRISE I and II is described in González-Bárcena et al. (2022).

For the CWS electronics unit we decided to work without a pressurised box, and to dissipate the power only by conduction and radiation. All electronics were designed for low power consumption and small power density to decrease or even avoid any hot spots. The advantages of a conduction cooled electronics unit in contrast to a pressurised box are reduced weight and a rather simple temperature control with heaters and radiation coolers. Furthermore, pressurised box and electronics designed to work under such pressure pose the risk of failure due to loss of air pressure. To protect all components from environmental influences, we applied an electrical isolation and hydrophobic coating to all boards. The cooling elements had a white coating with high emissivity and low absorption (MAP SG121FD). The power consumption of the CWS electronics unit in the operating mode is about 70 W, of which 56 W are used by the real time VPX6 computer board doing the wave-front correction.

In order to check the thermal behaviour especially of the E-Unit which has the highest power consumption, a thermal FEM model of the CWS has been created (as an example, see the temperature distribution of the E-Unit in Fig. 8). The modeling results show that every part is inside the expected operational temperatures. This was confirmed by a four-day thermal vacuum test at 5 mbar pressure which showed full functionality between -30 and $+40^{\circ}\text{C}$ ambient temperature. During the short flight in 2022 all CWS temperature sensors reported temperatures well inside the operational regime, both during the ascent phase and at flight altitude.

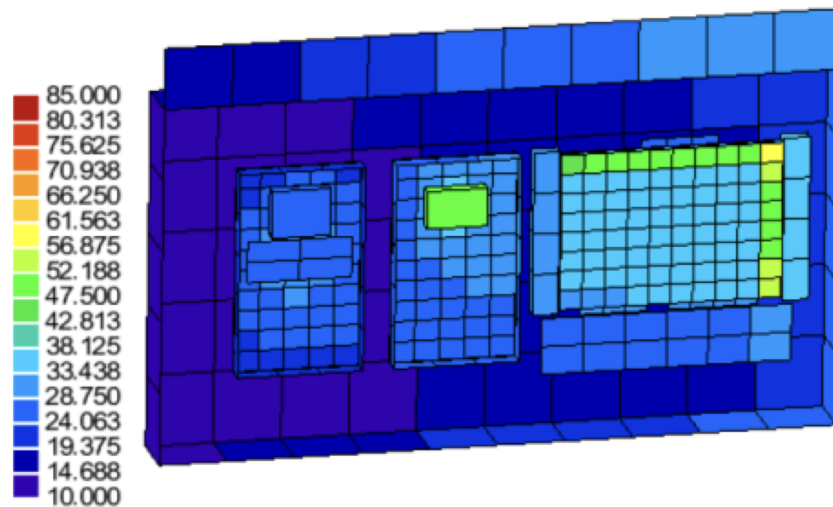


Figure 8. simulated temperature distribution (in deg C) of the E-Unit under flight conditions and in operation. From left to right: amplifier for the tip-tilt piezo drive, the system power supply and the VPX6 computer board. All temperatures are inside the operational limits.

6. Performance

The most important performance parameter of the SUNRISE III CWS is the attenuation factor for the tip-tilt correction. Residual image motions over a broad frequency range, from the gondola pendulum motion in the 0.1 Hz range to high-speed vibrations up to 200 Hz, are reduced by this factor. Figure 9 shows the attenuation factors of the tip-tilt error as a function of the disturbance frequency measured during the integration of the system by applying a sine voltage to a second tip-tilt mirror which acted as an error source. The black curve denotes the performance of the old SUNRISE I and II mirror mount, the red and blue curves resemble the SUNRISE III mirror mount.

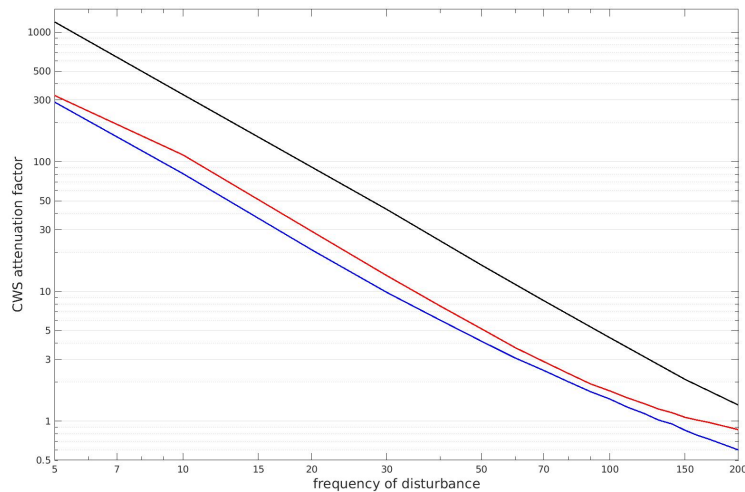


Figure 9. CWS SUNRISE III attenuation factor of the tip-tilt correction as a function of the frequency of the disturbance. *Black*: tip-tilt mirror mount used in SUNRISE I and II (both axes), *blue*: flight model used in SUNRISE III, axis 1, *red*: flight model used in SUNRISE III, axis 2.

The new SUNRISE III tip-tilt mount is optimised for a small (and constant) wavefront error under varying heat load, at the expense of a somewhat lower correction 0 db bandwidth of 130 Hz (axis 1) and 160 Hz (axis 2), as compared to the 230 Hz bandwidth when using the old SUNRISE I and II mount (both axes). As a result, the error attenuation when using the SUNRISE III mount is lower by a factor of 3 and 2.5, respectively, as compared to the SUNRISE I and II mount. This behaviour is also reflected in the Proportional-Integral-Derivative (PID) servo parameters which had to be adapted to a slower servo response. The derivative (D)-part had to be turned down to almost zero.

Nevertheless, the bandwidth of the SUNRISE III tip-tilt correction is higher than the 90 Hz of SUNRISE I and SUNRISE II, and much higher than the initial (insufficient) 30 Hz specification originating from SUNRISE I.

Figure 10 shows the in-flight residual RMS tip-tilt jitter at the science focus as measured by the CWS. It is obvious that the tilt axis performs much better than the tip axis. High speed telemetry showed the occurrence of hard external "shocks"

which resulted in tip-tilt excursions of up to one arcsecond. The five milli-arcsecond specification is often met by the tilt-axis, but not by the tip-axis.

During the last day of the flight, the gondola used softer control parameters which then transmitted less high frequency disturbances through the telescope. As can be seen in Fig. 10, this resulted in an overall better image stabilisation at the science focus.

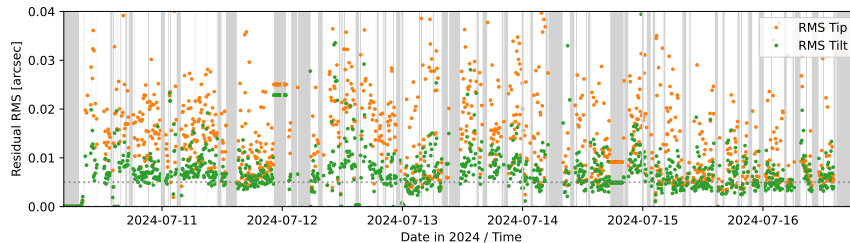


Figure 10. SUNRISE III residual (after correction) RMS image jitter as seen by the CWS as a function of time for tip (red) and tilt (green) axes. The grey areas denote times when the CWS correction was off. The dotted horizontal line shows the 5 milliarcseconds specification.

7. Conclusion

The image stabilisation system consisting of gondola and CWS played a crucial role for the success of the 2024 SUNRISE III flight. During the six-day flight, more than 200 TByte of high quality science data have been recorded.

To our knowledge, SUNRISE III has achieved the best image stabilization for balloon-borne mission to date. Other missions achieved, for example, down to 0.05'' RMS over half an hour (Balloon-borne Imaging Testbed, Romualdez et al. 2017) or 0.067'' RMS (Balloon Observation Platform for Planetary Science (BOPPS), Dankanich et al. 2013). The possibility of stabilising a meter-class balloon-borne telescope down to a few milliarcseconds opens the opportunity for future similar sized (and possibly even larger) balloon-borne telescopes, both for solar and night-time observations.

Acknowledgments We thank the Max Planck Institut für Sonnensystemforschung for their financial support. A special thanks goes to the employees of CSBF and Esrange / SSC for their support and hospitality during the launch campaigns. We thank our workshops for their excellent work and F. Krämer for support during the flight.

Funding SUNRISE III is supported by funding from the Max-Planck-Förderstiftung (Max Planck Foundation), NASA under Grant #80NSSC18K0934 and #80NSSC24M0024 (“Heliophysics Low Cost Access to Space” program), and the ISAS/JAXA Small Mission-of-Opportunity program and JSPS KAKENHI JP18H05234/JP23H01220. This research has received financial support from the European Union’s Horizon 2020 research and innovation program under grant agreement No. 824135 (SOLARNET) and No. 101097844 (WINSUN) from the European Research Council (ERC). It has also been funded by the Deutsches Zentrum für Luft- und Raumfahrt e.V. (DLR, grant no. 50 OO 1608). The Spanish contributions have been funded by the Spanish MCIN/AEI under projects RTI2018-096886-B-C5, and PID2021-125325OB-C5, and from “Center of Excellence Severo Ochoa” awards to IAA-CSIC (SEV-2017-0709, CEX2021-001131-S), all co-funded by European REDEF funds, “A way of making Europe”.

D. Orozco Suárez acknowledges financial support from a *Ramón y Cajal* fellowship. The research activities and the flight operation of M. Kubo were supported from the JSPS KAKENHI grants No. 23KJ0299, No. 24K07105, No. 23K13152, and No. 21K13972, respectively.

References

- Barthol, P., Gandorfer, A., Solanki, S.K., Schüssler, M., Chares, B., Curdt, W., Deutsch, W., Feller, A., Germerott, D., Grauf, B., Heerlein, K., Hirzberger, J., Kolleck, M., Meller, R., Müller, R., Riethmüller, T.L., Tomasch, G., Knölker, M., Lites, B.W., Card, G., Elmore, D., Fox, J., Lecinski, A., Nelson, P., Summers, R., Watt, A., Martínez Pillet, V., Bonet, J.A., Schmidt, W., Berkefeld, T., Title, A.M., Domingo, V., Gasent Blesa, J.L., Del Toro Iniesta, J.C., López Jiménez, A., Álvarez-Herrero, A., Sabau-Graziati, L., Widani, C., Haberler, P., Härtel, K., Kampf, D., Levin, T., Pérez Grande, I., Sanz-Andrés, A., Schmidt, E.: 2011, The Sunrise Mission. *Solar Phys.* **268**, 1. DOI. ADS.
- Berkefeld, T., Schmidt, D., Soltau, D., von der Lühe, O., Heidecke, F.: 2012, The GREGOR adaptive optics system. *Astronomische Nachrichten* **333**, 863. DOI. ADS.
- Berkefeld, T., Schmidt, W., Soltau, D., Bell, A., Doerr, H.P., Feger, B., Friedlein, R., Gerber, K., Heidecke, F., Kentischer, T., v. D. Lühe, O., Sigwarth, M., Wälde, E., Barthol, P., Deutsch, W., Gandorfer, A., Germerott, D., Grauf, B., Meller, R., Álvarez-Herrero, A., Knölker, M., Martínez Pillet, V., Solanki, S.K., Title, A.M.: 2011, The Wave-Front Correction System for the Sunrise Balloon-Borne Solar Observatory. *Solar Phys.* **268**, 103. DOI. ADS.
- Bernasconi, P., Carpenter, M., Eaton, H., Schulze, E., Carkhuff, B., Palo, G., Young, D., Raouafi, N., Vourlidis, A., Coker, R., Solanki, S.K., Korpi-Lagg, A., Gandorfer, A., Feller, A., Riethmüller, T.L., Smitha, H.N., Grauf, B., del Toro Iniesta, J.C., Orozco Suárez, D., Katsukawa, Y., Kubo, M., Berkefeld, T., Bell, A., Álvarez-Herrero, A., Martínez Pillet, V.: 2025, The Gondola for the SUNRISE III Balloon-Borne Solar Observatory. *Solar Phys.* **300**, 112. DOI. ADS.
- Dankanich, J., Kremic, T., Hibbitts, K., Young, E., Landis, R.: 2013, Planetary Science Balloon Based Platform Assessment.
- del Toro Iniesta, J.C., Orozco Suárez, D., Álvarez-Herrero, A., Sanchis Kilders, E., Pérez-Grande, I., B., R., Bellot Rubio, L.R., Balaguer Jiménez, M., López Jiménez, A.C., Álvarez García, D., Ramos Más, J.L., Cobos Carrascosa, J.P., Labrousse, P., Moreno Mantas, A.J., Morales-Fernández, J.M., Aparicio del Moral, B., Sánchez Gómez, A., Bailón Martínez, E., Bailén Martínez, F.J., Strecker, H., Siu-Tapia, A.L., Santamarina Guerrero, P., Moreno Vacas, A., Atiénzar García, J., Dorantes Monteagudo, A.J., Bustamante, I., Tobaruela, A., Fernández-Medina, A.B., Núñez Peral, A., Cebollero, M., Garranzo-García, D., García Parejo, P., Gonzalo Melchor, A., Sánchez Rodríguez, A., Campos-Jara, A., Laguna, H., Silva-López, M., Blanco Rodríguez, J., Gasent Blesa, J.L., Rodríguez Martínez, P., Ferreres, A., Gilabert Palmer, D., Torralbo, I., Piqueras, J., González-Bárcena, D., Fernandes, A.J., Hernández Expósito, D., Páez Mañá, E., Magdaleno Castillo, E., Rodríguez Valido, M., Korpi-Lagg, A., Gandorfer, A., Solanki, S.K., Berkefeld, T., Bernasconi, P., Feller, A., Katsukawa, Y., Riethmüller, T.L., Smitha, H.N., Kubo, M., Martínez Pillet, V., Grauf, B., Bell, A., Carpenter, M.: 2025, TuMag: the tunable magnetograph for the Sunrise III mission. *Solar Phys.* **300**. Part of the Topical Collection "The Sunrise III Solar Observatory".
- Feller, A., Gandorfer, A., Grauf, B., Hölken, J., Iglesias, F.A., Korpi-Lagg, A., Riethmüller, T.L., Staub, J., Fernandez-Rico, G., Castellanos Durán, J.S., Solanki, S.K., Smitha, H.N., Sant, K., Barthol, P., Bayon Laguna, M., Bergmann, M., Bischoff, J., Bochmann, J., Bruns, S., Deutsch, W., Eberhardt, M., Enge, R., Goodyear, S., Heerlein, K., Heinrichs, J., Hirche, D., Meining, S., Mende, R., Meyer, S., Mühlhaus, M., Müller, M.F., Monecke, M., Oberdorfer, D., Papagiannaki, I., Ramanath, S., Vergöhl, M., Vukadinović, D., Werner, S., Zerr, A., Berkefeld, T., Bernasconi, P., Katsukawa, Y., del Toro Iniesta, J.C., Bell, A., Carpenter, M., Álvarez Herrero, A., Kubo, M., Martínez Pillet, V., Orozco Suárez, D.: 2025, The Sunrise Ultraviolet Spectropolarimeter and Imager: Instrument Description. *Solar Phys.* **300**, 65. DOI. ADS.
- Gandorfer, A., Grauf, B., Barthol, P., Riethmüller, T.L., Solanki, S.K., Chares, B., Deutsch, W., Ebert, S., Feller, A., Germerott, D., Heerlein, K., Heinrichs, J., Hirche, D., Hirzberger, J., Kolleck, M., Meller, R., Müller, R., Schäfer, R., Tomasch, G., Knölker, M., Martínez Pillet, V., Bonet, J.A., Schmidt, W., Berkefeld, T., Feger, B., Heidecke, F., Soltau, D., Tischenberg, A., Fischer, A., Title, A., Anwand, H., Schmidt, E.: 2011, The Filter Imager SuFI and the Image Stabilization and Light Distribution System ISLiD of the Sunrise Balloon-Borne Observatory: Instrument Description. *Solar Phys.* **268**, 35. DOI. ADS.
- Gandorfer, A., Grauf, B., Staub, J., Bischoff, J., Woch, J., Hirzberger, J., Solanki, S.K., Álvarez-Herrero, A., García Parejo, P., Schmidt, W., Volkmer, R., Appourchaux, T., del Toro Iniesta, J.C.: 2018, The High Resolution Telescope (HRT) of the Polarimetric and Helioseismic Imager (PHI) onboard Solar Orbiter. In: Lystrup, M., MacEwen, H.A., Fazio, G.G., Batalha, N., Siegler, N., Tong, E.C. (eds.) *Space Telescopes and*

-
- Instrumentation 2018: Optical, Infrared, and Millimeter Wave, Society of Photo-Optical Instrumentation Engineers (SPIE) Conference Series* **10698**, 106984N. DOI. ADS.
- González-Bárcena, D., Fernández-Soler, A., González-Llana, A., Díez-González, J., Álvarez, R., Pérez-Grande, I., Sanz-Andrés, Á.: 2022, Ascent phase thermal analysis of Long Duration Balloons. *Acta Astronautica* **195**, 416. DOI. ADS.
- Katsukawa, Y., del Toro Iniesta, J.C., Solanki, S.K., Kubo, M., Hara, H., Shimizu, T., Oba, T., Kawabata, Y., Tsuzuki, T., Uraguchi, F., Shinoda, K., Tamura, T., Suematsu, Y., Matsumoto, T., Ishikawa, R.T., Naito, Y., Ichimoto, K., Nagata, S., Anan, T., Orozco Suárez, D., Balaguer Jiménez, M., López Jiménez, A.C., Quintero Noda, C., Álvarez García, D., Ramos Más, J.L., Aparicio del Moral, B., Sánchez Gómez, A., Hernández Expósito, D., Bailón Martínez, E., Morales Fernández, J.M., Moreno Mantas, A., Tobaruela, A., Bustamante, I., Piqueras, J., Pérez Grande, I., Korpi-Lagg, A., Gandorfer, A., Berkefeld, T., Bernasconi, P., Feller, A., Riethmüller, T.L., Smitha, H.N., Martínez Pillet, V., Grauf, B., Bell, A., Carpenter, M.: 2025, The Sunrise Chromospheric Infrared Spectro-Polarimeter SCIP: An Instrument for Sunrise III. *Solar Phys.* **300**. Part of the Topical Collection "The Sunrise III Solar Observatory".
- Korpi-Lagg, A., Gandorfer, A., Solanki, S.K., del Toro Iniesta, J.C., Katsukawa, Y., Bernasconi, P., Berkefeld, T., Feller, A., Riethmüller, T.L., Álvarez-Herrero, A., Kubo, M., Martínez Pillet, V., Smitha, H.N., Orozco Suárez, D., Grauf, B., Carpenter, M., Bell, A., Álvarez-Alonso, M.-T., Álvarez García, D., Aparicio del Moral, B., Atiénzar, J., Ayoub, D., Bailén, F.J., Bailón Martínez, E., Balaguer Jiménez, M., Barthol, P., Bayon Laguna, M., Bellot Rubio, L.R., Bergmann, M., Blanco Rodríguez, J., Bochmann, J., Borrero, J.M., Campos-Jara, A., Castellanos Durán, J.S., Cebollero, M., Conde Rodríguez, A., Deutsch, W., Eaton, H., Fernández-Medina, A.B., Fernandez-Rico, G., Ferreres, A., García, A., García Alarcia, R.M., García Parejo, P., Garranzo-García, D., Gasent Blesa, J., Gerber, K., Germerott, D., Gilbert Palmer, D., Gizon, L., Gómez Sánchez-Tirado, M.A., González-Bárcena, D., Gonzalo Melchor, A., Goodyear, S., Hara, H., Harnes, E., Heerlein, K., Heidecke, F., Heinrichs, J., Hernández Expósito, D., Hirzberger, J., Hoelken, J., Hyun, S., Iglesias, F.A., Ishikawa, R.T., Jeon, M., Kawabata, Y., Kolleck, M., Laguna, H., Lomas, J., López Jiménez, A.C., Manzano, P., Matsumoto, T., Mayo Turrado, D., Meierdierks, T., Meining, S., Monecke, M., Morales-Fernández, J., Moreno Mantas, A.J., Moreno Vacas, A., Müller, M.F., Müller, R., Naito, Y., Nakai, E., Núñez Peral, A., Oba, T., Palo, G., Pérez-Grande, I., Piqueras Carreño, J., Preis, T., Przybylski, D., Quintero Noda, C., Ramanath, S., Ramos Más, J.L., Raouafi, N., Rivas-Martínez, M.-J., Rodríguez Martínez, P., Rodríguez Valido, M., Ruiz Cobo, B., Sánchez Rodríguez, A., Sanchez Toledo, M., Sánchez Gómez, A., Sanchis Kilders, E., Sant, K., Santamarina Guerrero, P., Schulze, E., Shimizu, T., Silva-López, M., Singh, K., Siu-Tapia, A.L., Sonner, T., Staub, J., Strecker, H., Tobaruela, A., Torralbo, I., Tritschler, A., Tsuzuki, T., Uraguchi, F., Volkmer, R., Vourlidis, A., Vukadinović, D., Werner, S., Zerr, A.: 2025, Sunrise iii: Overview of Observatory and Instruments. *Solar Physics* **300**, 75. Part of the Topical Collection "The Sunrise III Solar Observatory". ISBN 1573-093X. DOI. URL.
- Martínez Pillet, V., Del Toro Iniesta, J.C., Álvarez-Herrero, A., Domingo, V., Bonet, J.A., González Fernández, L., López Jiménez, A., Pastor, C., Gasent Blesa, J.L., Mellado, P., Piqueras, J., Aparicio, B., Balaguer, M., Ballesteros, E., Belenguer, T., Bellot Rubio, L.R., Berkefeld, T., Collados, M., Deutsch, W., Feller, A., Girela, F., Grauf, B., Heredero, R.L., Herranz, M., Jerónimo, J.M., Laguna, H., Meller, R., Menéndez, M., Morales, R., Orozco Suárez, D., Ramos, G., Reina, M., Ramos, J.L., Rodríguez, P., Sánchez, A., Uribe-Patarroyo, N., Barthol, P., Gandorfer, A., Knoelker, M., Schmidt, W., Solanki, S.K., Vargas Domínguez, S.: 2011, The Imaging Magnetograph eXperiment (IMaX) for the Sunrise Balloon-Borne Solar Observatory. *Solar Phys.* **268**, 57. DOI. ADS.
- Michau, V., Marais, T., Laurent, J., Primot, J., Fontanella, J.-C., Tallon, M., Fuensalida, J.J.: 1991, High-resolution astronomical observations using deconvolution from wavefront sensing. In: Bissonnette, L.R., Miller, W.B. (eds.) *Propagation Engineering: Fourth in a Series, Society of Photo-Optical Instrumentation Engineers (SPIE) Conference Series* **1487**, 64. DOI. ADS.
- Müller, D., St. Cyr, O.C., Zouganelis, I., Gilbert, H.R., Marsden, R., Nieves-Chinchilla, T., Antonucci, E., Auchère, F., Berghmans, D., Horbury, T.S., Howard, R.A., Krucker, S., Maksimovic, M., Owen, C.J., Rochus, P., Rodríguez-Pacheco, J., Romoli, M., Solanki, S.K., Bruno, R., Carlsson, M., Fludra, A., Harra, L., Hassler, D.M., Livi, S., Louarn, P., Peter, H., Schühle, U., Teriaca, L., del Toro Iniesta, J.C., Wimmer-Schweingruber, R.F., Marsch, E., Velli, M., De Groof, A., Walsh, A., Williams, D.: 2020, The Solar Orbiter mission. Science overview. *Astron. Astrophys.* **642**, A1. DOI. ADS.
- Romualdez, L.J., Damaren, C.J., Li, L., Galloway, M.N., Hartley, J.W., Netterfield, C.B., Clark, P., Massey, R.J.: 2017, Precise pointing and stabilization performance for the balloon-borne imaging testbed: 2015 test flight. *Proceedings of the Institution of Mechanical Engineers, Part G: Journal of Aerospace Engineering* **231**, 713. DOI. URL.
- Scharmer, G.B., Löfdahl, M.G., van Werkhoven, T.I.M., de la Cruz Rodríguez, J.: 2010, High-order aberration compensation with multi-frame blind deconvolution and phase diversity image restoration techniques. *Astron. Astrophys.* **521**, A68. DOI. ADS.

-
- Solanki, S.K., Barthol, P., Danilovic, S., Feller, A., Gandorfer, A., Hirzberger, J., Riethmüller, T.L., Schüssler, M., Bonet, J.A., Martínez Pillet, V., del Toro Iniesta, J.C., Domingo, V., Palacios, J., Knölker, M., Bello González, N., Berkefeld, T., Franz, M., Schmidt, W., Title, A.M.: 2010, SUNRISE: Instrument, Mission, Data, and First Results. *Astrophys. J. Lett.* **723**, L127. DOI. ADS.
- Solanki, S.K., Riethmüller, T.L., Barthol, P., Danilovic, S., Deutsch, W., Doerr, H.-P., Feller, A., Gandorfer, A., Germerott, D., Gizon, L., Grauf, B., Heerlein, K., Hirzberger, J., Kolleck, M., Lagg, A., Meller, R., Tomasch, G., van Noort, M., Blanco Rodríguez, J., Gasent Blesa, J.L., Balaguer Jiménez, M., Del Toro Iniesta, J.C., López Jiménez, A.C., Orozco Suarez, D., Berkefeld, T., Halbgewachs, C., Schmidt, W., Álvarez-Herrero, A., Sabau-Graziati, L., Pérez Grand e, I., Martínez Pillet, V., Card, G., Centeno, R., Knölker, M., Lecinski, A.: 2017, The Second Flight of the Sunrise Balloon-borne Solar Observatory: Overview of Instrument Updates, the Flight, the Data and First Results. *Astrophys. J. Lett. Suppl.* **229**, 2. DOI. ADS.
- Solanki, S.K., del Toro Iniesta, J.C., Woch, J., Gandorfer, A., Hirzberger, J., Álvarez-Herrero, A., Appourchaux, T., Martínez Pillet, V., Pérez-Grande, I., Sanchis Kilders, E., Schmidt, W., Gómez Cama, J.M., Michalik, H., Deutsch, W., Fernandez-Rico, G., Grauf, B., Gizon, L., Heerlein, K., Kolleck, M., Lagg, A., Meller, R., Müller, R., Schühle, U., Staub, J., Albert, K., Alvarez Copano, M., Beckmann, U., Bischoff, J., Busse, D., Enge, R., Frahm, S., Germerott, D., Guerrero, L., Löptien, B., Meierdierks, T., Oberdorfer, D., Papagiannaki, I., Ramanath, S., Schou, J., Werner, S., Yang, D., Zerr, A., Bergmann, M., Bochmann, J., Heinrichs, J., Meyer, S., Monecke, M., Müller, M.-F., Sperling, M., Álvarez García, D., Aparicio, B., Balaguer Jiménez, M., Bellot Rubio, L.R., Cobos Carracosa, J.P., Girela, F., Hernández Expósito, D., Herranz, M., Labrousse, P., López Jiménez, A., Orozco Suárez, D., Ramos, J.L., Barandiarán, J., Bastide, L., Campuzano, C., Cebollero, M., Dávila, B., Fernández-Medina, A., García Parejo, P., Garranzo-García, D., Laguna, H., Martín, J.A., Navarro, R., Núñez Peral, A., Royo, M., Sánchez, A., Silva-López, M., Vera, I., Villanueva, J., Fourmond, J.-J., de Galarreta, C.R., Bouzit, M., Hervier, V., Le Clec'h, J.C., Szvec, N., Chaigneau, M., Buttice, V., Dominguez-Tagle, C., Philippon, A., Boumier, P., Le Cogneu, R., Baranjuk, G., Bell, A., Berkefeld, T., Baumgartner, J., Heidecke, F., Maue, T., Nakai, E., Scheiffelen, T., Sigwarth, M., Soltau, D., Volkmer, R., Blanco Rodríguez, J., Domingo, V., Ferreres Sabater, A., Gasent Blesa, J.L., Rodríguez Martínez, P., Osorno Caudel, D., Bosch, J., Casas, A., Carmona, M., Herms, A., Roma, D., Alonso, G., Gómez-Sanjuan, A., Piqueras, J., Torralbo, I., Fiethe, B., Guan, Y., Lange, T., Michel, H., Bonet, J.A., Fahmy, S., Müller, D., Zouganelis, I.: 2020, The Polarimetric and Helioseismic Imager on Solar Orbiter. *Astron. Astrophys.* **642**, A11. DOI. ADS.